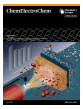

Elucidating the Performance Limitations of Alkaline Electrolyte Membrane Electrolysis: Dominance of Anion Concentration in Membrane Electrode Assembly

Fatemeh Razmjooei,*[a] Azharuddin Farooqui,[a] Regine Reissner,[a] Aldo Saul Gago,[a] Syed Asif Ansar,[a] and Kaspar Andreas Friedrich[a, b]

Anion exchange membrane water electrolyzers (AEMWEs) offer a cost-effective technology for producing green hydrogen. Here, an AEMWE with atmospheric plasma spray non-precious metal electrodes was tested in 0.1 to 1.0 M KOH solution, correlating performance with KOH concentration systematically. The highest cell performance was achieved at 1.0 M KOH (ca. 0.4 A cm^{-2} at 1.80 V), which was close to a traditional alkaline electrolysis cell with ≈6.0 M KOH. The cell exhibited 0.13 V improvement in the performance in 0.30 M KOH compared with 0.10 M KOH at 0.5 A cm^{-2}. However, this improvement becomes more limited when further increasing the KOH concentration. Electrochemical impedance and numerical simulation results show that the ohmic resistance from the membrane was the most notable limiting factor to operate in low KOH concentration and the most sensitive to the changes in KOH concentration at 0.5 A cm^{-2}. It is suggested that the effect of activation loss is more dominant at lower current densities; however, the ohmic loss is the most limiting factor at higher current densities, which is a current range of interest for industrial applications.

1. Introduction

Electrolytic production of hydrogen from water as an alternative energy carrier to fossil fuels has attracted a plethora of attention in the context of sustainability, renewable energy source utilization and green technology.[1–10] Currently, there are two main types of low-temperature water electrolysis available for commercial deployment: conventional alkaline water electrolysis (AWE) and proton exchange membrane water electrolysis (PEMWE).[11–13] One of the main advantages of AWE over PEMWE is the substitution of conventional noble metal electrocatalysts with active, stable and relatively low-cost transition metal catalysts for the hydrogen evolution reaction (HER) and oxygen evolution reaction (OER).[14] Therefore, AWEs are considered as the least costly technologies for water electrolysis.[15,16] However, the highly concentrated KOH solution (up to 10.0 M KOH) in these systems, which requires a recirculation with adequate cleaning leads to the formation of insoluble species like K_2CO_3, which precipitates in the pores of the catalyst layers limiting the transport of reactants and products and causing low cell performance.[6,7]

Another disadvantage of AWE compared to PEMWE is related to the higher system complexity with electrolyte recirculation and a higher effort for system start up from cold standby. In AWE, cathode and anode are separated by a thick diaphragm, which limits the transport of ions to the electrodes at the same rate. This effect results in unequal pressure at both electrode sides,[7] causing gas crossover.[17] Introducing a solid polymer electrolyte membrane can offer several advantages compared to the conventional AWE including a wider range of operation, higher purity of gases, increased efficiency and rapid system response and compactness.[18–20] Thus, anion exchange membrane water electrolysis (AEMWE) has the potential to combine the low costs of AWE,[21] with some of the advantages offered by PEMWE.[18] However, new anion exchange membranes (AEMs) with internal high pH are necessary. Such AEMs have been applied for alkaline fuel cell technology but comparatively in water electrolyzers have been rarely used.[7,18,22] The few studies on AEMWE show that the cell performance is still much lower than that of PEMWE due to: i) lack of very highly hydroxide conductive membranes,[18] and ii) slower kinetics of HER in neutral and alkaline condition.[23,24] These reactions are considered to be pH-dependent, thus they improve by increasing the pH.[23,24] Therefore, a wide range of non-precious metal-based catalysts, which show high performance in the conventional AWE with high concentrated KOH electrolyte, does not operate properly in AEMWE. To address this challenge, various cost-effective transition metal-based catalysts such as Ni/CeO_2–La_2O_3/C, NiFe, Ni and NiMo for the cathode, NiFe and $CuCoO_3$ for the anode, CoS_2-TiO_2 and NiFeS

[a] Dr. F. Razmjooei, Dr. A. Farooqui, R. Reissner, Dr. A. S. Gago, Dr. S. A. Ansar, Prof. K. A. Friedrich
Institute of Engineering Thermodynamics
German Aerospace Center (DLR)
Pfaffenwaldring 38–40, Stuttgart, 70569, Germany
E-mail: Fatemeh.Razmjooei@dlr.de
[b] Prof. K. A. Friedrich
Institute of Building Energetics, Thermal Engineering and Energy Storage (IGTE)
University of Stuttgart
Pfaffenwaldring 31, 70569, Stuttgart, Germany

Supporting information for this article is available on the WWW under https://doi.org/10.1002/celc.202000605

as bi-functional catalysts for both OER and HER have been reported.[6,15,16,25–32]

The membrane electrode assembly (MEA), which consists of two electrodes, the anode and the cathode separated by polymer electrolyte membrane, is typically made by two main routes. The first one consists of direct coating of catalysts layer (CL) in the form of ink onto the membrane by different techniques such as spraying, screen printing and electro-depositing, thus producing catalyst coated membrane (CCM). The MEA is subsequently made by compressing gas diffusion layers (GDL) or porous transport layers (PTL) on both sides of CCM. While this method has advantages for decreasing the contact resistance between the CL and the membrane, poor contact between the CL and the GDL can decline overall electrolyzer performance. Alternatively, MEAs can be made by direct coating of CL onto the GDLs, which is called gas diffusion electrodes (GDEs). However, it is reported that the solvent, which is used to prepare the catalyst ink can influence the surface morphology of the GDE by formation of cracks as a result of the drying process of the solvent.[33] Moreover, the binder of the catalyst is a source of degradation in operation.[34]

DLR has been therefore developing AEMWE having binder-and-solvent-free non-noble metal-based electrodes, namely NiAl as anode and NiAlMo as cathode on top of stainless steel-based PTLs by an atmospheric plasma spray (APS) deposition technique.[35] The process can be scaled readily to multi-m^2 sized electrodes and integrated with a fully automated assembly line. The MEA is simply fabricated by placing a commercial AEM between anode and cathode coated PTLs. This MEA manufacturing process avoids the difficulties in the CCM preparation, thus reducing the overall cost of AEMWE.

Herein, the APS NiAl and NiAlMo coated on PTLs are tested as anode and cathode, respectively, in an AEMWE with low concentrated KOH in the range of 0.10 M to 1.0 M KOH. Recently, DLR compared the performance of different APS-based anode materials, Ni/C, NiAl and NiAlMo along with the NiAlMo as a cathode in AEMWE only in the 1.0 M KOH using hexamethyl-p-terphenyl poly-184 (benzimidazolium) solid polymer electrolyte (HMT-PBI).[35] In the present work, The performance of current AEMWE with APS NiAl as an anode and NiAlMo as a cathode in 1.0 M KOH (1.8 V at a current density of $\approx$0.4 A cm^{-2}) is very close to the AEMWE performance in a recent report by DLR (1.8 V at a current density of 0.39 A cm^{-2}).[35] This shows a significantly high, reliable and reproducible performance of AEMWE using APS electrode packages in 1.0 M KOH. The performance of AEMWE with APS-based non-precious metal-based electrodes and AEM is comparable with or even better than the AEMWE with different non-precious-based catalysts and various AEMs in 1.0 M KOH, NiFeCo/NiFe/Sustainion ($\approx$0.49 A cm^{-2} at 1.80 V),[36] Acta 4030/Acta 3030/A-201 ($\approx$0.2 A cm^{-2} at 1.80 V),[37] NiFeCo/$NiFe_2O_4$/Sustainion ($\approx$0.49 A cm^{-2} at 1.80 V), FAS-50 ($\approx$0.23 A cm^{-2} at 1.80 V), FAPQ (less than 0.20 A cm^{-2} at 1.80 V), PBI (less than 0.20 A cm^{-2} at 1.80 V).[38] However, the main direction of development in AEMWE aims at using pure water or highly diluted KOH solution, typically 1.0 M KOH or less. Screening the literature, it seems obvious that AEMWEs operated with supporting electrolytes with higher electrolyte concentration show significantly better performance than those with only pure water caused by very low hydroxyl conductivity of current AEMs. However, this effect has not been systemically explored for AEMWE. In this work the effect of using different KOH concentrations (0.10 M to 1.0 M) on AEMWE performance was investigated in a systematic manner and was comprehensively studied. It is found that the cell performance improves with slight increase of KOH concentration due to the drastic reduction in ohmic resistance of the AEM and fast reaction kinetics of OER and HER. However, at the same time this improvement becomes more limited at moderately higher KOH concentration. Therefore, it is found that there is a compromise when increasing the KOH concentration, which should be taken into account for the design of AEMWE cells. Furthermore, in order to completely replace the supporting electrolyte with the pure water in AEMWE, beside highly active electrodes, the fabrication and implementation of a highly conductive and mechanically robust OH^- conducting membrane is highly demanded. To the best of our knowledge, this is the first study systemically investigating the effect of different KOH concentrations on the AEMWE performance. In addition, compared to other published reports,[35–38] the AEMWE of the current work also showed lower degradation of less than 2% over approximately 112 h of continuous chronopotentiometric operation at a constant current density of 0.5 A cm^{-2}, in 1.0 M KOH. Furthermore, no matter what concentration, highly concentrated KOH ($\approx$6.0 M) or slightly moderate concentrated KOH (1.0 M), the current APS-based electrodes are highly effective due to their low overpotential when used as OER and HER electrocatalyst to split water into O_2 and H_2. This provides a proof-of-concept that the APS technique is a reliable and trustworthy method to manufacture robust and highly active electrodes for AEMWE. The AEMWE reported in this study combines the benefits of PEMWE and AWE by using AEM and non-precious metal electrodes making this technology more efficient and suitable for large-scale applications.

2. Results and Discussion

The schematic illustration of the electrode fabrication and the recently developed in-house AEMWE configuration are depicted in Scheme 1. As can be seen in Scheme 1a, NiAl and NiAlMo alloys were deposited on top of the stainless steel-based PTL by spraying the NiAl and NiAlMo powder (Figure S1 of supporting information (SI) via the APS deposition method (Scheme 1a and 1b). Before the electrochemical test, to increase the porosity, less resistant aluminide phases to KOH solution and some unreacted metals partially were removed in a 30 wt.% KOH + 10 wt.% NaK-tartrate-tetrahydrate (complex-former) solutions for 24 h at 80 °C. The APS NiAl and NiAlMo with a geometrical active area of 4 cm^2 have been tested as an anode and a cathode, respectively, in AEMWE in very low concentrated KOH solutions (0.10 M to 1.0 M KOH). The samples before KOH activation are NiAl-BA and NiAlMo-BA and samples after KOH activation are NiAl-AA and NiAlMo-AA, where BA stands for

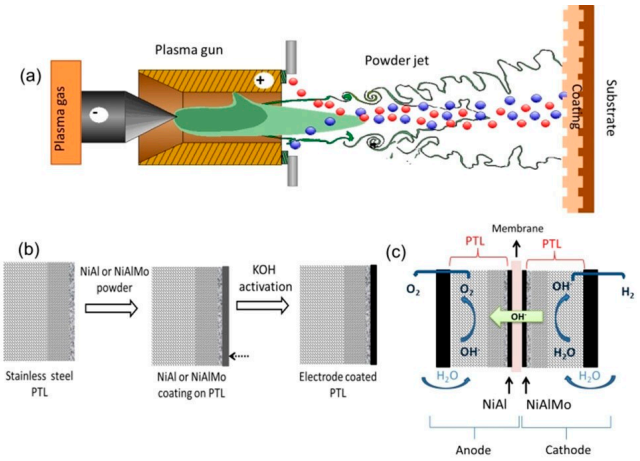

Scheme 1. a) Schematic illustration of plasma spraying, b) preparation steps of the catalyst coated PTLs, c) scheme of AEMWE with the catalyst coated PTLs.

before activation and AA stands for after activation. (For more details see Experimental part). As shown in Scheme 1c, the membrane is simply sandwiched between two coated PTLs, which act as binder-free catalyst layers as well as liquid/gas diffusion layer and current collector. To comprehend the effect of KOH activation on the crystal structure of the catalyst coated PTLs, the coated layers are analyzed by X-ray diffraction (XRD) analysis, before and after KOH activation. The comparative XRD patterns for NiAl-BA and NiAlMo-BA along with their activated counterparts (NiAl-AA and NiAlMo-AA) are shown in Figure 1a and 1b, respectively. As can be seen in Figure 1a, the phase constituent of the as-prepared APS NiAl consists of Ni_2Al_3 and $NiAl_3$. After KOH activation, the compound phase regarding the $NiAl_3$ is not found in the NiAl-AA and Ni_2Al_3 intensity decreases. This shows complete removal of $NiAl_3$ phase with higher Al:Ni $\approx$3 ratio and partial removal of Ni_2Al_3 phase with comparatively lower Al:Ni $\approx$1.5 ratio, suggesting easier removal of NiAl alloy rich in Al phase.[39]

As can be seen from the diffractograms in Figure 1b, the major constituents formed during plasma spraying of NiAlMo alloy on the PTL are the aluminides such as AlNi, Ni_2Al_3 and also different nickel and molybdenum phases such as $Mo_{1.08}Ni_{2.93}$ and MoNi. Some other peaks attributed to the Mo and Al_2O_3 are also observed. The peaks shown by black arrows could not be found in the XRD card number. However, the diffraction peaks shown by the black arrows have a similar pattern to the cubic phase of NiAl (PDF# 01-083-3994, space group Pm3 m) and the lattice spacings, d, for all those peaks are corresponding to a lattice parameter of around 2.93 Å, which is more than 1% larger than that of NiAl phase. This fact may suggest the inclusion and doping of Mo into the NiAl alloy.[40] However, the KOH activation leads to the removal of Mo and partially Ni_2Al_3 phases, which follows the same trend as the NiAl catalyst. The removal of some aluminide or metallic species during the KOH activation can generate pores in the catalyst backbone resulting in increased surface area. It is worth mentioning that after activation and removal of some species, the remaining peaks in the NiAl-AA and NiAlMo-AA compared to their unactivated ones shift to a lower angle, which can be due to the lattice distortion after activation.[41]

To investigate the topological features and properties of the prepared electrodes, the microstructures of the electrode surface before and after KOH activation were analyzed by scanning electron microscopy (SEM). SEM micrographs of NiAl and NiAlMo electrodes before and after activation are shown in Figure 2. Figure 2a presents the cross-sectional SEM image of NiAl package including the NiAl coating on the stainless steel-based PTL. Compared with the as-prepared catalyst, NiAl-BA, Figure 2b, the KOH activated sample, NiAl-AA (Figure 2c) shows a very porous sponge-like structure with several gaps between layers, which can be attributed to the removal of aluminide $NiAl_3$ and partially Ni_2Al_3 species during the KOH activation. Figure 2d shows the cross-sectional SEM images of the NiAlMo package including the NiAlMo coating on the stainless steel-based PTL. The SEM images of the as-sprayed NiAlMo sample and the activated one can be seen in Figure 2e and 2f, respectively. Significant differences in the electrode surface before and after KOH activation can be observed. As compared with NiAlMo-BA (Figure 2e), some pores are formed in NiAlMo-AA structure with a significantly larger area, Figure 2f. This can be due to the partially selective dissolution of aluminide phases such as Ni_2Al_3 and metallic species (Mo) by KOH activation.

These results are in good agreement with the XRD analysis. Therefore, after KOH activation a significant increase in the porosity is observed in both NiAl-AA and NiAlMo-AA samples.

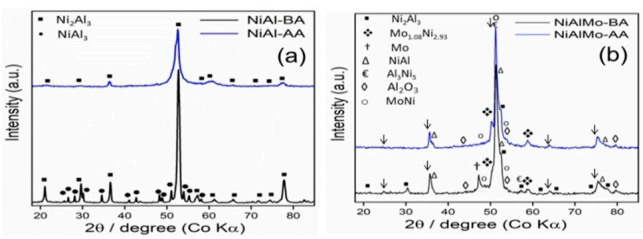

Figure 1. XRD patterns of APS a) NiAl electrode before and after activation; b) NiAlMo electrode before and after activation.

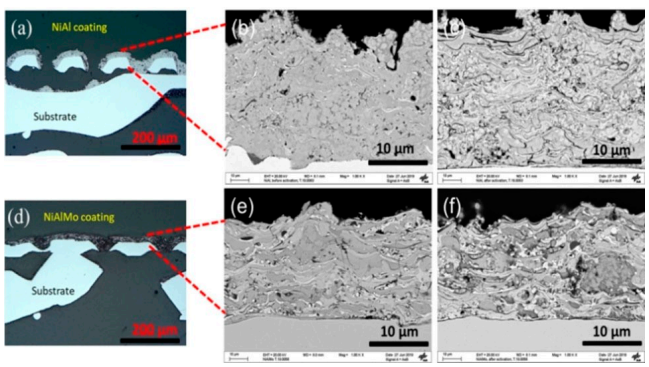

Figure 2. Cross-section SEM images of a) NiAl electrode coated on the stainless steel PTL, b) high-resolution NiAl-BA coating, c) high-resolution NiAl-AA coating, d) NiAlMo electrode coated on the stainless steel PTL, e) NiAlMo-BA and f) NiAlMo-AA.

Besides the presence of active sites in catalysts, their accessibility to the reactants is also crucial to ensure their utilization and capability of fulfilling their function as an OER or HER catalysts. Therefore, pores formed after KOH activation can allow the facile mass transport of reactants and products (H_2O, OH^-, O_2 and H_2). Additionally, the pores mitigate diffusion limitations and are favorable for easy formation of the interfacial area between active sites and reactants, eventually increasing the overall electrolyzer performance.[42]

The efficiency of leaching is confirmed by the energy-dispersive X-ray (EDX) spectroscopy measurements, Figure 3. As shown in Figure 3, elemental mapping images for NiAl and NiAlMo electrodes before and after activation indicate the existence of Ni, Al and O and Ni, Mo, Al and O, respectively. However, during the activation, Al components (green color) are partially etched off to form cavities and pores. The SEM images and their corresponding EDX elemental mapping (Ni, Al, Mo and O) images of the as-prepared NiAl and NiAlMo and their activated counterparts are shown with more details in Figure S2 of SI, the first and second rows, respectively. EDX elemental mapping images of NiAl before and after activation at the first and second rows, respectively, in Figure S2a and S2b of SI, indicate the existence of Ni, Al and O in the NiAl-BA catalyst. It can be seen that Al, which is shown in green color is partially leached out from 35.17 wt.% in NiAl-BA to 12.96 wt.% in NiAl-AA. However, some exposed Al, found in the surface and between the gaps was not removed by KOH activation. According to the XRD results, this Al can be in the form of Ni_2Al_3. Based on the XRD results, the leaching part can be due to the removal of $NiAl_3$ and partial removal of Ni_2Al_3. The SEM images and their corresponding elemental distribution in the as-prepared NiAlMo and its activated counterpart are shown in Figure S2c and S2d of SI, the third and fourth rows, respectively. As can be seen in Figure S2c of SI, the third rows, EDX elemental mapping images confirm the existence of Ni, Al, Mo and O in the as-prepared NiAlMo catalyst. However, after KOH activation, Al, which is shown in green color is partially leached out and decreases from 30.78 wt.% in NiAlMo-BA to 19.78 wt.% in NiAlMo-AA. According to the XRD analysis, this leached Al can be attributed to partial removal of Ni_2Al_3 phases. Furthermore, the remaining Al in the NiAlMo-AA catalyst backbone can be attributed to the NiAl, Al_3Ni_5 and MoNi, residual Ni_2Al_3 and also Al in the form of Al_2O_3, formed during the APS process, which are not dissolved in the KOH solution. The presence of Al_2O_3 can be observed by the light blue color in the EDX images in the oxygen mapping Figure S2d of SI, which is overlapping with the space covered with Al (green) in Figure S2d of SI, the fourth row. The amount of Mo also decreases from 21.34 wt.% for NiAlMo-BA to 16.87 wt.% for NiAlMo-AA. The leached out Mo originates from unreacted Mo. However, according to the XRD, the rest of Mo species, which remain in the NiAlMo-AA can be due to the reacted ones with Ni in the form of $Mo_{1.08}Ni_{2.93}$ and MoNi. The presence of $Mo_{1.08}Ni_{2.92}$ and MoNi can be observed by the light red color in the EDX images in Figure S2d of SI, the fourth row for nickel mapping, which is overlapping with the space covered with Mo (purple). After KOH activation, O content increases from 3.48 for NiAl-BA to 13.52 wt.% for NiAl-AA and from 5.47 for NiAlMo-BA to 13.42 wt.% for NiAlMo-AA. The initial presence of O can be due to plasma spraying in the air and an increase of O content after activation can be due to the OH^- adsorption during the KOH activation process and eventually the formation of Ni $(OH)_2$ and also catalyst surface passivation.[33–45]

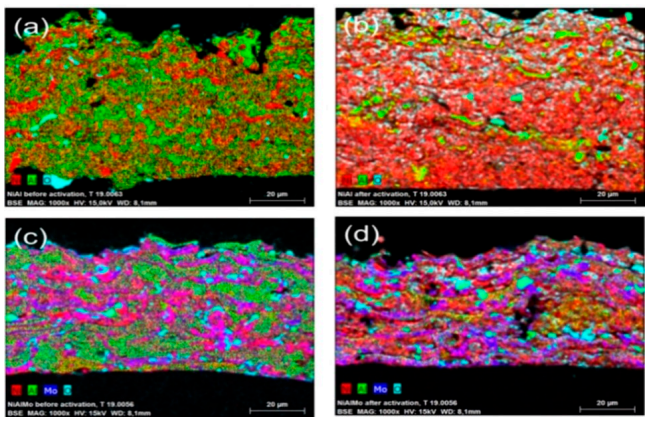

Figure 3. The corresponding element mapping images of a) NiAl-BA, b) NiAl-AA, c) NiAlMo-BA and d) NiAlMo-AA.

Electrochemical characterization was performed to investigate the influence of the different KOH concentration on the AEMWE performance. The performance of the single-cell based on the cell configuration with APS NiAl-AA anode, APS NiAlMo-AA cathode and AEM (NEOSEPTA) in terms of polarization curves are shown in Figure 4a. Figure 4a includes the plots for all cells in different diluted KOH concentration solutions (0.10 M to 1.0 M) at 65 °C. It can be seen that at higher KOH concentrations, overall cell performance is better over the

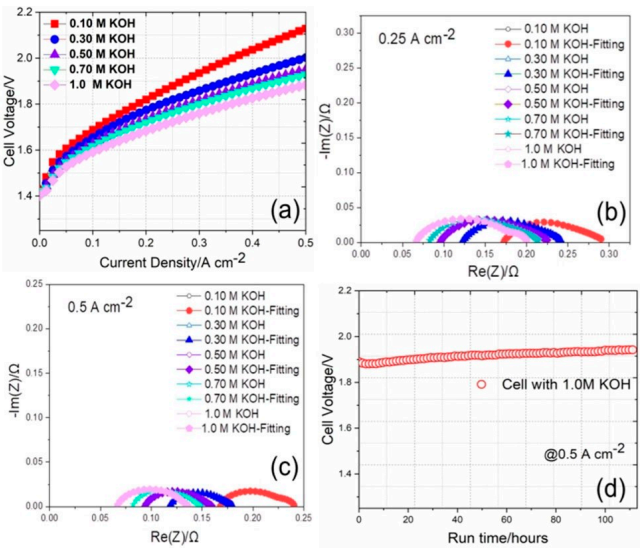

Figure 4. Electrochemical characterization of the AEMWE based on the cell configuration with APS NiAl-AA anode and APS NiAlMo-AA cathode in various KOH concentrations (0.10 to 1.0 M KOH) at 65 °C: a) polarization curves, b) Nyquist plots from the EIS measurements (from 100 kHz to 100 mHz) at 0.25 A cm^{-2}, c) EIS at 0.5 A cm^{-2} and d) chronoamperometric measurements at a constant current density 0.5 A cm^{-2} for AEMWE in 1.0 M KOH for 112 h.

whole range of applied current densities than the ones in low KOH concentrations. For example, the cell operated in 1.0 M KOH achieves a cell potential of 1.87 V at 0.5 A cm^{-2}, which shows an improvement of 0.25, 0.13, 0.08 and 0.05 V at the same current density compared to the cells operated at 0.10, 0.30, 0.50 and 0.70 M KOH, respectively.

It is evident from Figure S3 of SI that a significant activation improvement is obtained by utilizing high concentrated KOH solutions. This positive behavior is expected due to better reaction kinetics for both HER and OER,[23,24,46] better ion mobility and higher membrane conductivity in high concentrated KOH solutions compared with the diluted ones.[8,9] However, this positive enhancement in performance with increasing the KOH concentration is much more obvious at a lower concentrated solution. For example, the cell performance increases by lowering the cell potential by 0.13 V at 0.5 A cm^{-2} for 0.30 M KOH compared to 0.10 M KOH, although, increasing the KOH concentration from 0.30 M to 0.50 M leads to lowering the cell potential by only 0.050 V at 0.5 A cm^{-2}. The same trend is observed when changing the KOH concentration to 0.50 and 0.70 M. The cell performance improves with higher KOH concentrations due to the reduction in ohmic resistance of the AEM and fast reaction kinetics of OER and HER.[46,47] However, at the same time this improvement becomes more limited at high KOH concentration due to an increment in the viscosity, which results in gas bubble surface coverage and blockage of some of the active sites in the catalyst backbone.[8] Therefore, there is a compromise when increasing the KOH concentration, which should be taken into account for the design of AEMWE cells.

Electrochemical impedance spectroscopy (EIS) was systematically carried out to investigate further the effect of using different KOH concentrations at different current densities. Figures 4b, 4c and S4 of SI, show the impedance analysis together with their model fits as a Nyquist plot and obtained resistances for different KOH concentrations at 0.025, 0.25 and 0.5 A cm^{-2}. The equivalent circuit (Figure S4a of SI) consisted of lumped resistance (R) in series with two circuits, each comprising a resistance (R1 and R2) and a constant phase element (CPE1 and CPE2) in parallel to each other. The inductor (L) in series with the R represents possible inductive parts of cables and other components. The R or high frequency resistance (HFR), which appears as the intercepts of the Nyquist plot with the x-axis at high frequency (left side of Nyquist plot) represents the total area normalized internal ohmic resistance of the cell, which is expressed as the sum of the contributions from membrane resistance, material resistance of the cell components and contact resistances.[48] CPE1 and CPE2 are related to the double-layer capacitance for HER at the cathode and OER at the anode side. The polarization resistance, R1 and R2, are identified with the overall rate of the HER and OER and incorporates the charge transfer resistances of different step reactions during HER and OER.[49] The low frequency resistance (LFR) represents the intercepts of the Nyquist plot with the low frequency (right side of the Nyquist plot) includes the overall polarization resistance of the cell including the HFR parts.[50]

The impedance data collected at low current density 0.025 A cm^{-2}, Figure S4b of SI show that by increasing the KOH concentration, charge transfer resistance R1 does not change much but R2 increases moderately. In the assignment of the charge transfer resistances this indicates a decreased activity of OER with increasing KOH concentration. However, it is to be supposed that both HER and OER kinetic improve with increasing the KOH concertation, which should result in a reduction in activation loss.[51,52] This surprising observation for the OER can be explained when considering that increasing concentration of KOH also leads to an increased viscosity, which influences hydrodynamic transport properties, like diffusion, convection, but also bubble formation and bubble detachment.[53] Since we do not expect mass transport limitation to be significant at such low current densities we attribute the OER activity loss to the bubble formation on the electrode surface and partially active sites blockage by increasing the electrolyte viscosity at elevated KOH concentration.[54] Therefore, the increase in the electrolyte viscosity at low current densities might cause coalescence of bubbles and thus augmentation in the bubble size, which could cover the active electrode surface, leading to the activation loss.[54] However, as can be seen in Figure S4b of SI, at 0.025 A cm^{-2}, ohmic loss decreases with increasing the KOH concentration, which is commonly interpreted as a higher conductivity of the membrane . However, this effect saturates at higher KOH concentration even though electrolyte conductivity correlates linearly with KOH concentration in this range. Therefore, we can expect bubble formation to be also responsible for this saturation effect. The ohmic loss results from membrane and contact resistance. At elevated KOH concentrations more bubble formation occurred and the trapped bubbles between the electrode surface and membrane lead to less contact area. It is found that, at lower current densities activation loss is the most dominant factor for total cell performance.

At 0.25 A cm^{-2}, a very slight increment in charge transfer resistance was observed and at this range of current density ohmic resistance is the most dominant factor for the total cell performance, Figures 4b and S4c of SI. The impedance data collected at the current density of 0.5 A cm^{-2} shows that by increasing the KOH concentration, activation loss decreases slightly when KOH concentration increases from 0.10 M to 0.30 M. Subsecquently, it starts slightly increasing at higher KOH concentration, Figures 4c and 4Sd of SI, but the significance of this trend is doubtful. It is worth noting that ohmic resistance is the most dominant factor for total cell performance at 0.5 A cm^{-2}.

To see the effect of higher current densities on the impedance and cell performance, we also evaluated impedance data at 0.75 A cm^{-2}, Figure S5 of SI. From Figure 5S of SI, no influence of concentration on activation loss is seen at higher current densities. It is reported that the increase of current density brings down the critical diameter for bubble formation and caused the bubble departure from the electrode surface.[54] However, to meet this requirement, highly porous electrodes are needed to allow the passage of two phase liquid/gas with the driving force of high current density. Very high current densities can lead to two possible effects. The high voltage applied would result in local heating stemming from the ohmic

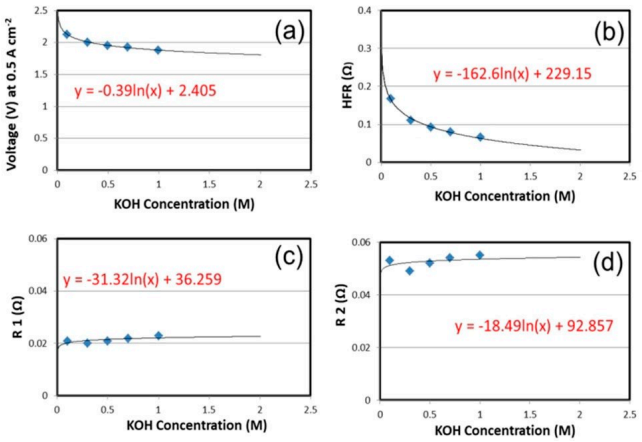

Figure 5. Logarithmic relationship of a) voltage at current density of 0.5 A cm^{-2}, b) HFR or ohmic resistance originating from membrane resistance, c) R1 originating from HER and d) R2 originating from OER versus the different KOH concentration.

loss at higher current densities. This localized heating in turns results in a temperature gradient on the electrode surface. Although, the more gas formed at higher current density, the localized heating might cause a reduction of the bubble size, which is a driving force for the bubble movement from the porous electrode surface.[54] Furthermore, at higher current densities, where gases produced at higher rates, bubble detachment is more effective and a well separated gas distribution in the pore systems may develop. At higher current densities enough driving force is applied to reduce the bubble coverage on the porous electrode surface, which in turns results in both activation and ohmic loss decrement at higher electrolyte viscosity. However, this improvement gets limited at higher KOH concentrations with more gas formation.

It is worth mentioning that, at each constant KOH concentration at higher current densities, ohmic loss raise from membrane conductivity is the most limiting factor for the overvoltage rather than activation loss. It can be seen from Figures 4b and 4c and Figure S4 of SI that both HFR and LFR decrease with increasing KOH concentration. However, the decrement in HFR and LFR is much more pronounced at lower KOH concentration. For example at 0.5 A cm^{-2}, the HFR and LFR drop 50 mΩ and 62 mΩ, respectively, for 0.30 M KOH compare to 0.10 M KOH. However, by further increasing the KOH concentration from 0.30 M to 0.50 M, the HFR and LFR drop only 23 mΩ and 18 mΩ, respectively. The same trend is observed with increasing further KOH concentration, which is in line with the findings from polarization curves. This can support the idea that while a higher concentration of KOH can decrease the ohmic resistance and improve somewhat both OER and HER kinetics, the increment is restricted at higher concentrated solution due to the higher amount of gas formation and the possibility of blockage of some of the active sites on the catalyst surface. It can be suggested that the effect of activation loss is more dominant at lower current densities while ohmic loss at medium and higher current densities. Therefore, since operating the electrolyzer at current densities of 200–500 mA cm^{-2} in the range of 1.8–2.4 V is industrial appealing range, we believe that reducing the the ohmic losses by decreasing the inhibiting bubble coverage can drastically improve cell performance at the current density of interest.

The stability of an AEMWE is an important factor for implementing this technology for profitable hydrogen production. The durability of a cell in 1.0 M KOH was evaluated under 0.5 A cm^{-2} at 65 °C and the cell voltage as a function of test time is shown in Figure 4d. As can be seen in Figure 4d, the cell exhibits durable operations over approximately 112 h of continuous chronopotentiometry. The increase in cell voltage is 350 μV/h, contributing to only 2% degradation under a very harsh condition.

This degradation rate is in a comparable range with or close to those of the reported AEMWEs with the commonly used AEM (28 μm thick A-201 and 9 μm thick A-901 membrane).[37,55] However, the currently available commercial AEMs used in AEMWE are still at an early stage of development and are not yet competitive to their counterparts, cationic exchange membrane in PEMWE. The good durability of a cell depends on the stability of membrane and appropriate contact between the catalyst layer and PTLs, which may prevent delamination of catalyst layer during durability test. The slight increase in the cell voltage from the durability test can be due to the formation of bubbles under the continuous operation at the high current density and blockage of some active sites or slightly loss of ion exchange capacity (IEC) in the membrane.

For comparison, the APS NiAl-AA anode and NiAlMo-AA cathode catalysts deposited on perforated nickel sheets have been tested in the AWE with ≈6.0 M KOH using Zirfon® separator. Perforated nickel substrate has been used for APS electrode fabrication for AWE, because Ni substrate is more resistant to corrosion than stainless steel substrate in a highly concentrated alkaline solution (≈6.0 M KOH). Figure S6 of SI shows the polarization curves of the conventional AWE cell based on the cell configuration with APS NiAl anode, APS NiAlMo cathode, and separator (Zirfon® separator) at 70 °C in ≈6.0 M KOH solution. The current density of 0.5 A cm^{-2} at 1.80 V was recorded as the initial performance in ≈6.0 M KOH solutions for AWE. The performance of AEMWE with the APS NiAl anode and NiAlMo cathode catalysts operated in 1.0 M KOH solution (≈0.4 A cm^{-2} at 1.80 V) at 65 °C is close to that of conventional AWE operated in even higher KOH concentration (≈6.0 M) and higher temperature (70 °C). The similar performance in AEMWE operated in low concentrated KOH with the AWE operated in high concentrated KOH can be attributed to appropriate hydroxyl ion conductivity of the AEM, eliminating the need for using a highly concentrated solution.

A set of formulae is delivered to transform changes including voltage at 0.5 A cm^{-2}, HFR, R1 and R2 into relative ones, allowing tracing the values for different KOH concentration with the current AEMWE cell. As can be seen in Figure 5a, initially the increase of the KOH concentration has a significant effect on the cell voltage, which initially shows a very sharp drop suggesting performance improvement by increasing initial KOH concentration. However, this behavior becomes more linear at the high concentrated KOH. This increment in

the performance can be due to the higher OER and HER kinetics and also higher membrane conductivity at elevated KOH concentration.

Though, all types of resistance (HFR, R1 and R2) initially show reduction with increasing KOH concentration from 0.10 to 0.30 M, HFR continued decreasing but by smaller rate, by further increasing KOH concentration, however, R1 and R2 slightly increased upon an increase of KOH concentration at 0.5 A cm^{-2}, which could be due to formation of bubbles and blockage of some of the active sites on the catalyst surface. It can be suggested that the effect of ohmic loss is the main limiting factor at a high current density of 0.5 A cm^{-2}, which is a current range of interest for industrial application. However, it is worth noting that the effect of KOH concentration on the overall cell resistance and consequently cell performance is more limited at higher KOH concentration than the lower ones. Therefore, to completely eliminate the usage of alkaline electrolyte, the highly hydroxyl conductive membrane is needed for AEMWE in which water electrolysis occurs in the high pH catalyst layers of MEA at the interface of catalysts and highly conductive membrane.

After the durability test, the samples were subjected to XRD and SEM/EDX analysis for determining the changes of phase and elemental composition. The electrode after the durability test named as NiAl-AT and NiAlMo-AT, where AT stands for after durability test. As can be seen in Figure 6a, the XRD pattern of NiAl electrode after durability test still not only shows peaks for Ni_2Al_3 but also indicates the formation of nickel oxide (PDF# 01-083-3994). The formation of nickel oxide after the durability test can be observed by the increase of light blue color in the EDX images in the oxygen mapping (Figure 6b), compare to that of NiAl before durability test (Figure S2b of SI), which is overlapping with the space covered with Ni (red). The increase in the oxygen content and formation of nickel oxide is due to the highly oxidative OER potential.

As can be seen in Figure 6c, the XRD pattern of NiAlMo-AT remains the same with the NiAlMo before the durability test (Figure 1b). However, the EDX analysis of NiAlMo-AT shown in Figure 6d, exhibits the increase of light blue color in the EDX images in the oxygen mapping compare to that of NiAlMo before durability test (Figure S2d of SI), which is overlapping with the space covered with Ni (red). The increase of O content can be due to the OH^- adsorption during the electrochemical testing and eventually formation of $Ni(OH)_2$.[43–45] However, as can be seen from SEM images in Figure S2b, S2d of SI and 6b and 6d, the sponge-like porous morphology of NiAl-AT and NiAlMo-AT electrodes is well retained after the durability test, despite partial oxidation and formation of partially Ni oxide or hydroxide, indicating the dimensional robustness of these electrodes.

Figure 7a, presents a comparison between the experimental and theoretical polarization data obtained for AEMWE cells with APS-based electrodes at different KOH concentrations. The model reproduces the effect shown in experimental data upon varying KOH concentration, supporting its validity . The percentage error of the present model is around 2%, which is acceptable. Basically, the role of the KOH is to reduce the power loss including both ohmic and activation losses driving the current through the solution and consequently improving the performance. As seen in Figure 7a, numerical results show that increasing the KOH concentration lowers voltage in the entire current density range. This positive behavior is expected due to better reaction kinetics for both HER and OER,[23,24,46] and improved membrane conductivity in higher concentrated KOH solution, Figure S7b of SI. The numerical analysis also shows that the increment in the cell performance with increasing the KOH concentration is much more significant at a lower concentrated solution, which is in good agreement with the experimental data. This increment is limited at higher KOH concentration due to the increment of viscosity, which results in gas bubble surface coverage and blockage of some of the active sites in the catalyst backbone.[8] Therefore, to evaluate

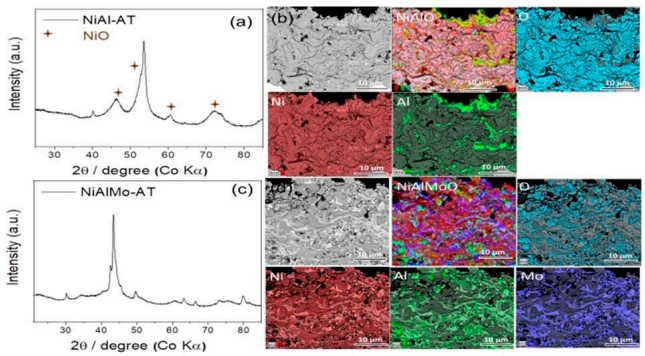

Figure 6. XRD patterns of the a) NiAl-AT and c) NiAlMo-AT electrodes after the 112 h durability test at 0.5 A cm^{-2} in 1.0 M KOH. SEM images and the corresponding element mapping images of b) NiAl-AT and d) NiAlMo-AT electrodes after the 112 h durability test at 0.5 A cm^{-2} in 1.0 M KOH.

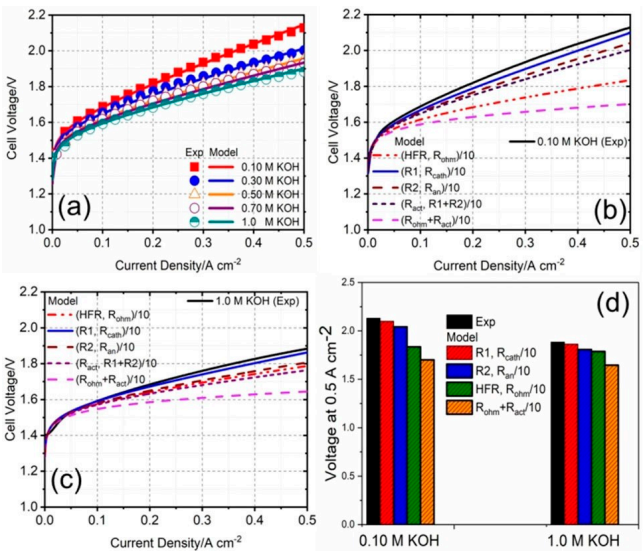

Figure 7. a) Comparison between the numerical results and experimental data. The sensitivity of AEMWE electrolyzer model to the ohmic and activation resistance decreased by a factor of 10 in b) 0.10 M KOH, c) 1.0 M KOH, d) comparison of the sensitivity of AEMWE electrolyzer model for both 0.10 M and 1.0 M KOH when ohmic and activation resistance decreased by a factor of 10.

the effect of membrane conductivity and OER and HER kinetics, the membrane resistance and both cathodic and anodic resistances are decreased by a factor of 10 at both 0.10 M and 1.0 M KOHcalled improved cells, Figure 7b-d,. As shown in Figure 7b–d, the performance of AEMWE improved by minimizing the various losses in the cell at both 0.10 M and 1.0 M KOH. However, as numerical results show, reducing the ohmic loss originated from the membrane resistance plays the most important role for increasing the overall cell performance in both 0.10 M and 1.0 M KOH.This effect is more significant in lower KOH concentration, 0.1 M KOH rather than 1.0 M KOH. The same trend is also observed for the cathodic and anodic reactions, though with a smaller fraction. From Figure 7d, by assuming the total resistance decrement including decreasing the membrane resistance and both cathodic and anodic resistances by factor of 10, the cell performance increased 27% compared to the experimental data at 1.0 M KOH.Moreover, by assuming the same condition, the cell performance increased 45% compared to the experimental data at 0.1 M KOH reaching almost the same performance of the improved cell in 1.0 M KOH. This results from the simulation suggests that to achieve a high performance in much more diluted alkaline solution, or pure water a highly hydroxyl conductive membrane remains top priority. Furthermore, not only the development of highly active electrode for OER but also the development of highly active electrode for HER becomes critical for fulfilling this requirement.

3. Conclusions

In summary, non-noble metal-based MEAs for AEMWE were fabricated with APS electrodes and commercial membrane and tested in various KOH concentrations from 0.10 to 1.0 M. The cathode and anode were NiAlMo and NiAl alloys, respectively. The highest increase in performance was achieved when changing the KOH solution from 0.10 to 0.30 M. This beneficial effect is less pronounced for KOH concentrations above 0.30 M due to the increase in viscosity and generation of a large number of gas bubbles, which limit the access of reactants to the active sites of the catalyst layer. Impedance results show that among all losses, the ohmic resistance from the membrane was the most notable limiting factor to operate in low KOH and also the most sensitive to the changes in the KOH concentration at the high current density of 0.5 $A\,cm^{-2}$, which is a current range of interest for industrial application. It is suggested that the effect of activation loss is more dominant at lower current densities; however, the ohmic loss is the most limiting factor at higher current densities, which are a current range of interest for industrial application. The ohmic and charge transfer resistances of OER and HER reached a minimum with 1.0 M KOH. At this concentration the cell achieved a current density of $\approx$0.4 $A\,cm^{-2}$ at 1.80 V, which is very close to the one, 0.5 $A\,cm^{-2}$ at 1.80 V, in $\approx$6.0 M KOH achieved in AWE. Furthermore, SEM/EDX analysis showed that the sponge porous morphology of NiAl-AT and NiAlMo-AT electrodes are well retained after durability test, despite the formation of partial Ni oxide or hydroxide, indicating the dimensional robustness of these electrodes. This in turns helps to retain 98% of its initial cell performance after the 112 h durability test, representing a novel prime example of HER and OER electrodes for the AEMWE application. Thus, the use of an AEM with appropriate ion conductivity and highly active and durable plasma sprayed-electrodes eliminates the need for using highly concentrated KOH solutions in alkaline electrolysis.

Experimental Section

APS-Based Electrode Fabrication

The electrodes were produced by spraying powders of NiAl or NiAlMo supplied by HC Stack on porous stainless steel multi-mesh structures, PTL, by APS. A Triplex-Pro210 plasma gun from Oerlikon-Metco (CH) is used for APS for which Ar is the primary plasma forming gas and H_2 and/or He are used as secondary gases. The spray powder (Figure S1 of SI) is injected through external injection nozzles into the plasma jet, where particles were accelerated and heated due to momentum and heat transfer between plasma and particles and the quasi or fully molten particles impacted the substrate surface, flattened, solidified and consolidated to form an electrode coating. Multiple layers are coated to form electrodes of suitable thickness. Key information is summarized in Table S1 of SI. Before, the electrochemical test, to increase the porosity, less resistant aluminide phases to KOH solution and some unreacted metals partially is removed in a 30 wt.% KOH + 10 wt.% NaK-tartrate (complex-former) solutions for 24 h at 80 °C. The samples before KOH activation are NiAl-BA and NiAlMo-BA and samples after KOH activation are NiAl-AA and NiAlMo-AA, where BA stands for before activation and AA stands for after activation. The electrode after the durability test named as NiAL-AT and NiAlMo-AT, where AT stands for after testing.

Physical Characterization

XRD patterns of the coating samples were acquired using an X-ray diffractometer STADI P (STOE, Germany) in the Bragg-Brentano geometry with Co–Kα source operated at 40 kV and 30 mA. To fix samples for further analysis such as SEM and EDX, the samples are made into the resin. The applied resin is the mixture of resin and hardener with a mass ratio of 25:3. After mixing the resin components for several minutes, the bubbles produced during mixing will be forced out with the help of a vacuum pump. The coated PTLs are placed in the mold and the resin mixture is poured into the mound to cover all the samples followed by drying in ambient temperature for 8 hours. Before the physical characterization the resin samples are polished using different grinding size 46 μm, 22 μm, 15 μm, 9 μm and 3 μm to make the surface smoother and clearer. The morphology of the polished resin samples was observed with SEM using a Zeiss Gemini Ultra plus microscope operated at an acceleration voltage of 120 kV. The chemical compositions of the samples were determined by the EDX spectrometer/detector from the Bruker company.

Cell Assembly and Electrochemical Analysis

The KOH activated NiAl and NiAlMo with 4 cm^2 active areas are used as the anode and cathode, respectively. AEM (NEOSEPTA) available from Astom, which is pre-treated with 1.0 M KOH for 24 h and then washed with DI water, is placed between two coated PTLs. These coated PTLs also can act as both the gas diffusion layer

and the current collector. The stainless steel bipolar plates has been used for both cathode and anode sides. The cells were characterized in different KOH concentration solutions (0.10 to 1.0 M) at 65 °C by recoding polarization curves up to 0.5 A cm^{-2} with the slow scan rate of 10 mA s^{-1}, after 30 min activation at constant current 0.05 A cm^{-2}. EIS was performed from 100 kHz to 100 mHz at 1 A cm^{-2} with an amplitude of 100 mA, respectively, using a potentiostat/galvanostat (VSP-300) and booster (potentiostat/galvanostat Booster Board 10 A). In the case of AWE, both APS NiAl and NiAlMo alloys deposited on perforated nickel sheet with an active geometrical area of 4 cm^2 were placed on both side of Zirfon® separator. A knitted nickel wire structure is used as transport and contacting layer (thickness compressed approx. 1.5 mm). End plates on both sides were nickel foils with an area of 8.3 cm^2. The components are clamped together in the home made setup with stainless steel screws and (≈6.0 M) is fed to anode and cathode side. The test is performed at 70 °C. The current-voltage curve is measured galvanostatically with a Zahner Elektrik IM-6ex potentiostat up to 0.5 A cm^{-2}.

Modelling and Simulation of AEMWE Cell

Mathematical modelling as an effectual tool can play a significant role in evaluating the complicated physicochemical processes.[56] Herein, we develop a mathematical model for the AEMWE by considering the intricate physicochemical process including charge transport and electrochemical reaction at both anode and cathode sides. For simplicity, the formulation will be confined to a one-dimensional configuration. The model includes the fundamental equation considering thermodynamics of the system, electrochemical reaction kinetics and the losses in the electrical equivalent circuit. The cell voltage V_{cell}, which is a measure of the total amount of electrical energy demand for water splitting, results of the sum of the reversible voltage V_{rev} and all irreversible losses within the cell, Equation (1):[57,58]

$$V_{cell} = V_{rev} + V_{act} + V_{ohm} \tag{1}$$

The cell voltage which is the sum of reversible cell voltage, activation overpotential (anode and cathode overpotential) and ohmic overpotential is defined by equation (1). The reversible potential is reported to be calculated from the thermodynamics of the water dissociation reaction at standard temperature and pressure conditions given by Equation (2).[59]

$$V_{T,P}^{rev} = -\Delta G_{T,p}/nF = V_{T,P^0}^{rev} + \frac{RT}{nF}\ln\left[(p-\rho_w)^{1.5}\,\frac{\rho_w^*}{\rho_w}\right] \tag{2}$$

where, n is the number of electrons participating in the electrode reaction, G is the Gibbs free energy, F is the Faraday constant, V_{T,p^0}^{rev} is a reversible potential at given STP conditions, ρ_w is the partial pressure of gaseous electrolyte solution and $\rho_w{}^*$ is a partial pressure of pure water, R is the universal gas constant equals to 8.315 J/mol K and T is the temperature in Kelvin. V_{T,p^0}^{rev} at a given STP conditions can be calculated by Equation (3);[59]

$$V_{T,P^0}^{rev} = 1.50342 - 9.956\times10^{-4}\,T + 2.5\times10^{-7}\,T^2 \tag{3}$$

The partial pressure of gaseous electrolyte solution p_w in contact with gas products can be evaluated from the $p_w{}^*$ of pure water at the same temperature, Equations (4) and (5).[59–61]

$$p_w = \exp(37.93 - 6426.32/T).\exp(0.016214 - 0.13802 + 0.19330\sqrt{M})T^{-3.498} \tag{4}$$

$$p_w^* = \exp(37.043 - 6275.32/T)T^{-3.498} \tag{5}$$

where, M is the molarity of the solution and T is the absolute temperature.

The activation overpotential due to electrochemical reaction kinetics depends on temperature, nature of electrodes and the electrolyte composition. It follows Arrhenius law and expressed by the Butler-Volmer equation for redox reaction in the electrochemical cell given by Equation (6).[56]

$$i = i_0\left[\exp\left(\frac{\alpha}{RT}\,nFV_{act}\right) - \exp\left(\frac{(1-\alpha)}{RT}\,nFV_{act}\right)\right] \tag{6}$$

where, i is the current density and i_0 is the exchange current density at equilibrium, α is the charge-transfer coefficients, which describes the share of the energy barrier between the electrodes. For larger over potential voltages, the second term in equation (6) becomes negligible and the Butler-Volmer equation of (7) would be approximated to Tafel Equation (7);[62,63]

$$V_{act} = V_{act}^a + V_{act}^c = 2.3026\,\frac{RT}{nF\alpha_a}\log\left(\frac{i}{i_{0-a}}\right) + 2.3026\frac{RT}{nF\alpha_C}\,\log\left(\frac{i}{i_{0-c}}\right) \tag{7}$$

Exchange current density is related to the characteristics of the electrodes such as materials, geometry, and roughness. The charge transfer coefficients (α_a and α_c) are usually between 0.2 to 0.8 and for these experimental models it was found to be ≅0.67–70.[63,64] the exchange current densities for NiAl and NiAlMo obtained at different KOH concentration (0.1 to 1.0 M) using three-electrode system measurement, Figure S7a of SI.

The ionic conductivity of membrane for through-plane is given by Equation (8) where the R is the membrane resistance (Ω cm^2) and L is the thickness of the membrane and A is the area of the membrane.[65,66]

$$\sigma = \frac{L}{RA} \tag{8}$$

The conductivity of the Neosepta membrane with a thickness of 0.22 mm is evaluated for different KOH concentration, Figure S7b of SI.[67] The conductivity increases with the increase of KOH concentration as per Equation (9)

$$\sigma = [M]^{0.2196}\exp(\ln(I) + 0.56) \tag{9}$$

Acknowledgements

The authors thank Dr. Noriko Sata (DLR Stuttgart) for her support on XRD analysis, Ina Plock (DLR Stuttgart) for her support on SEM analysis, Mr. Volker Thielke (DLR Stuttgart) for his support on plasma spraying, Mr. Günter Roth (DLR Stuttgart) for his support on metallographic analysis, and Mr. Jörg Bürkle (DLR Stuttgart) for his assistance during experimental works. Open access funding enabled and organized by Projekt DEAL.

Conflict of Interest

The authors declare no conflict of interest.

Keywords: plasma spray · anion exchange membranes · electrolyzers · KOH concentration · electrodes

[1] F. Razmjooei, K. P. Singh, D. S. Yang, W. Cui, Y. Hee Jang, J.-S. Yu, *ACS Catal.* **2017**, *7*, 2381–2391.
[2] X. Wu, K. A. Scott, *J. Power Source* **2012**, *214*, 124–129.
[3] Y.-C. Cao, X. Wu, K. A. Scott, *Int. J. Hydrogen Energy* **2012**, *37*, 9524–9528.
[4] K. E. Ayers, E. B. Anderson, C. B. Capuano, M. Niedzweicki, M. Hickner, C.-Y. Wang, Y. Len, W. Zhou, *ECS Trans.* **2013**, *45*, 121–130.
[5] T. Pandiarajan, L. John Berchmans, S. Ravichandran, *RSC Adv.* **2015**, *5*, 34100–34108.
[6] I. Ulusoy, A. Uzunoglu, A. Ata, O. Ozturk, M. Ider, *ECS Trans.* **2009**, *19*, 77–94.
[7] Y. Leng, G. Chen, A. J. Mendoza, T. B. Tighe, M. A. Hickner, C.-Y. Wang, *JACS* **2012**, *134*, 9054–9057.
[8] F. Razmjooei, T. Liu, D. A. Azevedo, E. Hadjixenophontos, R. Reissner, G. Schiller, S. A. Ansar, K. A. Friedrich, *Sci. Rep* **2020**, 10, 10948.
[9] L. M. Gandía, R. Oroz, A. Ursu, P. Sanchis, P. M. Dieguez, *Energy Fuels* **2007**, *21*, 1699–1706.
[10] K. P. Singh, C.-H. Shin, H.-Y. Lee, F. Razmjooei, A. Sinhamahapatra, J. Kang, J.-S. Yu, *ACS Appl. Nano Mater.* **2020**, *3*, 3634–3645.
[11] G. Schiller, R. Henne, P. Mohr, V. Peinecke, *Int. J. Hydrogen Energy* **1998**, *23*, 761–765.
[12] S. A. Grigoriev, V. I. Porembsky, V. N. Fateev, *Int. J. Hydrogen Energy* **2006**, *31*, 171–175.
[13] S. Shiva Kumar, V. Himabindu, *Mater. Sci. Technol.* **2019**, *2*, 442–454.
[14] R. Phillips, C. W. Dunnill, *RSC Adv.* **2016**, *6*, 100643–100651.
[15] P. Ganesan, A. Sivanantham, S. Shanmugam, *J. Mater. Chem. A* **2018**, *6*, 1075–1085.
[16] P. Ganesan, A. Sivanantham, S. Shanmugam, *J. Mater. Chem. A* **2016**, *4*, 16394–16402.
[17] M. Mamoon Rashid, M. K. Al Mesfer, H. Naseem, M. Danish, *IJEAT* **2015**, *4*, 2249–8958.
[18] I. Vincent, D. Bessarabov, *Renewable Sustainable Energy Rev.* **2018**, *81*, 1690–1704.
[19] Q. Shi, C. Zhu, D. Dua Y Lin, *Chem. Soc. Rev.* **2019**, *48*, 3181–3192.
[20] S. Shiva Kumar, V. Himabindu, *Mater. Sci. Technol.* **2019**, *2*, 442–454.
[21] M. R. Kraglund, D. Aili, K. Jankova, E. Christensen, Q. Li, J. O. Jensen, *JES* **2016**, *163*, F3125-F3131.
[22] D. R. Dekel, *J. Power Sources* **2018**, 375, 158–169.
[23] J. Huang, P. Li, S. Chen, *J. Phys. Chem. C* **2019**, *28*, 17325–17334.
[24] J. Wei, M. Zhou, A. Long, Y. Xue, H. Liao, C. Wei, Z. J. Xu, *Nano-Micro Lett.* **2018**, *10*, 1.
[25] A. Y. Faid, A. O. Barnett, F. Seland, S. Sunde, *Catalysts* **2018**, *8*, 614.
[26] C. C. Pavel, F. Cecconi, C. Emiliani, S. Santiccioli A Scaffidi, *Angew. Chem. Int. Ed.* **2014**, *53*, 1378–1381; *Angew. Chem.* **2014**, *126*, 1402–1405.
[27] Y.-C. Cao, X. Wu, K. A. Scott, *Int. J. Hydrogen Energy* **2012**, *37*, 9524–9528.
[28] B. Dong, X. Zhao, G. Q. Han, X. Li, X. Shang, Y. R. Liu, W.-H. Hu, Y.-M. Chai, H. Zhao, C.-G. Liu *J. Mater. Chem. A*, **2016**, 4, 13499–13508.
[29] X. Wu, K. Scott, *J. Mater. Chem.* **2011**, *21*, 12344–12351.
[30] S. Seetharaman, R. Balaji, K. Ramya, K. S. Dhathathreyan, M. Velan, *Int. J. Hydrogen Energy* **2013**, *38*, 14934–14942.
[31] D. Li, I. Matanovic, A. S. Lee, E. J. Park, C. Fujimoto, H. T. Chung, S. Kim, *ACS Appl. Mater. Interfaces* **2019**, *11*, 10, 9696–9701.
[32] L. An, T. S. Zhao, Z. H. Chai, P. Tan, L. Zeng, *Int. J. Hydrogen Energy* **2014**, *39*, 19869–19876.
[33] J. Hack, T. M. M. Heenan, F. Iacoviello, N. Mansor, Q. Meyer, P. Shearing, N. Brandon, D. J. L. Brett, *J. Electrochem. Soc.* **2018**, *165*, F3045-F3052.
[34] J. Parrondo, C. G. Arges, M. Niedzwiecki, E. B. Anderson, K. E. Ayers, V. Ramani, *RSC Adv.* **2014**, *4*, 9875–9879.
[35] Li. Wang, T. Weissbach, R. Reissner, A. Ansar, A. S. Gago, S. Holdcroft, K. A. Friedrich, *ACS Appl. Energy Mater.* **2019**, *11*, 7903–7912.
[36] J. J. Kaczur, H. Yang, Z. Liu, S. D. Sajjad, R. I. Masel, *Front. Chem.* **2018**, *6*, 263.
[37] I. Vincent, A. Kruger, D. Bessarabov, *Int. J. Hydrogen Energy*, **2017**, 42, 10752–10761.
[38] Z. Liu, S. D. Sajjad, Y. Gao, H. Yang, J. J. Kaczur, R. I. Masel, *Int. J. Hydrogen Energy* **2017**, *42*, 29661–29655.
[39] Md.A. Rahman, X. Zhu, C. Wen, *Int. J. Electrochem. Sci.* **2015**, *10*, 3767–3783.
[40] R. Karmakar, S. K. Neogi, A. Banerjee, S. Bandyopadhyay, *Physica E Low Dimens Syst Nanostruct.* **2012**, *263*, 671–677.
[41] Z. Ul Abideen, F. Teng, *CrystEngComm* **2018**, *20*, 7866–7879.
[42] X. Zheng, J. Wu, X. Cao, J. Abbott, C. Jin, H. Wang, P. Strasser, R. Yang, X. Chen, G. Wu, *Appl. Catal. B* **2019**, *241*, 442–451.
[43] A. Mazzi, M. Orlandi, N. Bazzanella, Y. J. Popat, L. Minati, G. Speranza, A. Miotello, *Mat Sci Semicon Proc.* **2019**, *97*, 29.
[44] F. Razmjooei, C. Park, J.-S. Yu, *ChemElectroChem.* **2018**, *5*, 1985–1994.
[45] K. Juodkazis, J. Juodkazytė, R. Vilkauskaitė, V. Jasulaitienė, *J. Solid State Electrochem.*, **2008**, 12, 1469–1479.
[46] X. Ge, A. Sumboja, D. Wu, T. An, B. Li, F. W. T. Goh, T. S. Andy Hor, Y. Zong, Z. Liu, *ACS Catal.* **2015**, *5*, 4643–4667.
[47] M. K. Kraglund, M. Carmo, G. Schiller, S. A. Ansar, D. Aili, E. Christensen, J. O. Jensen, *Energy Environ. Sci.* **2019**, *12*, 3313–3318.
[48] S. H. Frensch, A. C. Olesen, S. S. Araya, S. K. Kær, *Electrochim. Acta* **2018**, *263*, 228–236.
[49] S. Siracusano, S. Trocino, N. Briguglio, V. Baglio, A. S. Aricò, *Materials.* **2018**, *11*, 1368.
[50] P. Lettenmeier, S. Kolb, N. Sata, A. Fallisch, L. Zielke, S. Thiele, A. S. Gago, K. A. Friedrich, *Energy Environ. Sci.* **2017**, *10*, 2521–2533.
[51] G.-F. Li, M. Divinagracia, M. F. Labata, J. D. Ocon, P.-Y. Abel Chuang, *ACS Appl. Mater. Interfaces* **2019**, *11*, 33748–33758.
[52] X. Wang, C. Xu, M. Jaroniec, Y. Zheng, S.-Z. Qiao, *Nat. Commun.* **2019**, *10*, 4876.
[53] J. C. Garcia-Navarro, M. Schulze, K. A. Friedrich, *ACS Sustainable Chem. Eng.* **2019**, *7*, 1600–1610.
[54] D. Zhang, K. Zeng, *Ind. Eng. Chem. Res.* **2012**, *51*, 13825–13832.
[55] I. Vincent, A. Kruger, D. Bessarabov, *Int. J. Electrochem. Sci.*, **2018**, 13, 11347–11358.
[56] L. An, T. S. Zhao, Z. H. Chai, P. Tan, L. Zeng, *Int. J. Hydrogen Energy* **2014**, *39*, 19869–19876.
[57] M. Carmo, D. L. Fritz, *Int. J. Hydrogen Energy* **2013**, *38*, 4901–4934.
[58] B. Han, S. M. S. Iii, J. Mo, F. Zhang, *Int. J. Hydrogen Energy* **2015**, *40*, 7006–7016.
[59] J. Milewski, G. Guandalini, S. Campanari, *J. Power Sources* **2014**, 269, 203–211.
[60] K. Zouhri, S. Lee, *Int. J. Hydrogen Energy* **2016**, *41*, 7253–7263.
[61] M. Hammoudi, C. Henao, K. Agbossou, Y. Dube, M. Doumbia, *Int. J. Hydrogen Energy* **2012**, *37*, 13895–13913.
[62] B. Han, S. M. S. Iii, J. Mo, F. Zhang, *Int. J. Hydrogen Energy* **2015**, *40*, 7006–7016.
[63] A. Roy, S. Watson, D. Infield, *Int. J. Hydrogen Energy.* **2006**, *31*, 1964–1979.
[64] T. Shinagawa, A. T. Garcia-esparza, K. Takanabe, *Nat. Publ. Gr.* **2015**, *5*, 13801.
[65] D. Tang, J. Lu, L. Zhuang, *J. Electroanal. Chem.* **2010**, *644*, 144–149.
[66] J. Koettgen, M. Martin, *J. Am. Ceram. Soc.* **2020**, *103*, 3776–3787.
[67] J. Hnát, M. Paidar, J. Schauer, J. Žitka, K. Bouzek, Par, *J. Appl. Electrochem.* **2012**, *42*, 545–554.

Manuscript received: April 28, 2020
Revised manuscript received: July 7, 2020